Vacuum ultraviolet excited state dynamics of small amides

Vacuum Ultraviolet Excited State Dynamics of Small Amides

Martin A. B. Larsen[1,a] and Theis I. Sølling[1]

[1]*Department of Chemistry, University of Copenhagen, 2100 Copenhagen Ø, Denmark*

Ruaridh Forbes[2,3,a], Andrey E. Boguslavskiy[3,4], Varun Makhija[3], Kévin Veyrinas[3,b], Rune Lausten[4] and Albert Stolow[3,4,5,c]

[2]*Department of Physics and Astronomy, University College London, Gower Street, London, WC1E 6BT, UK*

[3]*Department of Physics, University of Ottawa, 150 Louis Pasteur, Ottawa, ON, K1N 6N5, Canada*

[4]*National Research Council Canada, 100 Sussex Drive, Ottawa, ON, K1N 5A2, Canada*

[5]*Department of Chemistry, University of Ottawa, 10 Marie Curie, Ottawa, ON K1N 6N5, Canada*

Magdalena M. Zawadzki[6,a], Lisa Saalbach[6,a], Nikoleta Kotsina[6], Martin J. Paterson[7] and Dave Townsend[6,7,c]

[6]*Institute of Photonics & Quantum Sciences, Heriot-Watt University, Edinburgh, EH14 4AS, UK*

[7]*Institute of Chemical Sciences, Heriot-Watt University, Edinburgh, EH14 4AS, UK*

Abstract

Time-resolved photoelectron spectroscopy in combination with *ab initio* quantum chemistry calculations was used to study ultrafast excited state dynamics in formamide (FOR), *N,N*-dimethylformamide (DMF) and *N,N*-dimethylacetamide (DMA) following 160 nm excitation. A particular focus was on internal conversion processes within the excited state Rydberg manifold and how this behavior in amides compared with previous observations in small amines. All three amides exhibited extremely rapid (<100 fs) evolution from the Franck-Condon region. We argue that this is then followed by dissociation. Our calculations indicate subtle differences in how the excited state dynamics are mediated in DMA/DMF as compared to FOR. We suggest that future studies employing longer pump laser wavelengths will be useful for discerning these differences.

Keywords: Time-resolved photoelectron spectroscopy, amides, Rydberg-valence mixing, velocity-map imaging, vacuum ultraviolet.

---

[a] *Joint lead investigators.*

[b] *Present address: Centre Lasers Intenses et Applications (CELIA), Domaine du Haut Carré, 43 rue Pierre Noailles, 33405 Talence Cedex, France.*

[c] *Corresponding authors: d.townsend@hw.ac.uk, astolow@uottawa.ca*

This manuscript was accepted by J. Chem. Phys. Click here to see the version of record.

I. INTRODUCTION

Amine- and amide-based motifs occur frequently in important biomolecular systems such as amino acids, peptides, the DNA bases and plant phenylpropanoids. Developing a better understanding of the physical and chemical role these small sub-units play within the larger biological environment is therefore of considerable significance. One key characteristic is their resistance to damage following ultraviolet (UV) absorption. Mechanisms facilitating excess energy redistribution within electronically excited amine and amide chromophores are therefore of much interest and a common theme in many investigations is the role played by low-lying singlet excited states of mixed Rydberg/valence composition.[1, 2] Such states are now known to be common to a broad range of small hetero-atom containing systems, typically exhibiting predominantly 3s orbital character in the Franck-Condon region but developing σ* valence character as N-H, O-H or S-H bonds are extended. Mixed Rydberg/valence states therefore potentially act as "dynamical doorways" for non-adiabatic radiationless transitions back to the S_0 ground state.[3] UV photoprotection mechanisms are based on the excess ground state vibrational energy being then dissipated harmlessly into the surroundings.

The evolution of 3s Rydberg to σ* valence character has been the subject of extensive study, as illustrated, for example, in detailed reviews by Ashfold *et al.*[1] and Roberts and Stavros.[2] Recent time-resolved photoelectron imaging measurements concluded, however, that the very long (>10 ps) excited state lifetimes seen in a series of tertiary *aliphatic* (i.e. unsaturated) amines are a consequence of the 3s state in these systems avoiding σ* valence character. In contrast, secondary and primary aliphatic amines exhibit sub-picosecond decay of the 3s state, as σ* valence character readily develops at extended N–H distances.[4-6] This is illustrated, for example, when comparing dynamics observed in piperidine (a secondary aliphatic amine) and *N*-methylpyrrolidine (a tertiary species). In both cases, excitation at 200

This manuscript was accepted by J. Chem. Phys. Click here to see the version of record.

nm populates a member of the 3p Rydberg manifold, which is followed by rapid (<400 fs) internal conversion to the 3s state. This subsequently decays in <200 fs in piperidine and 160 ps in *N*-methylpyrrolidine. Supporting *ab initio* calculations also indicate differences in Rydberg state evolution of valence character in tertiary versus secondary/primary aliphatic amines. In both systems, members of the 3p manifold (but not the 3s state) appear to develop σ* character upon N-C bond extension (a factor mediating the aforementioned 3p to 3s internal conversion). In contrast, 3s to σ* evolution is only seen along N-H bonds (a coordinate absent in tertiary species). Expanded discussions of this effect may be found elsewhere.[4-6]

The situation outlined above is complicated further by the fact that *aromatic* amines display different behavioral trends. Here, 3s Rydberg states in both tertiary and primary/secondary systems appear able to develop σ* character at extended N-H or N-CH_3 distances. This is highlighted, for example, in recent TRPEI work comparing *N,N*-dimethylaniline (a tertiary system) with aniline and 3,5-dimethylaniline (primary systems).[7, 8] The introduction of π-bonding and conjugation therefore appears to exert significant new influences over electronic state character as a function of nuclear coordinates. This idea is further reinforced by recent preliminary theoretical investigations exploring the effect of unsaturated chemical functionality on Rydberg-to-valence evolution within a series of model amine systems.[8] Systematic placement of C=C double bonds in close proximity to the amine N atom centre appears to modify dynamical behavior in tertiary species, with 3s to σ* evolution beginning to occur as states of ππ* character intersect the Rydberg manifold. Similar proximity effects have recently been argued in the non-adiabatic dynamics of acrylonitrile and its methyl-substituted derivatives.[9]

In the following, we present a time-resolved photoelectron spectroscopy (TRPES) study of the non-adiabatic processes operating in formamide (FOR), *N,N*-dimethylformamide

This manuscript was accepted by J. Chem. Phys. Click here to see the version of record.

(DMF) and *N,N*-dimethylacetamide (DMA), schematic structures of which are illustrated in Fig. 1. The dynamical influence exerted by the proximity of the carbonyl C=O group to the N-H_2 or N-$(CH_3)_2$ centres was investigated at a vacuum ultraviolet (VUV) pump wavelength centered at 159.4 nm (7.78 eV). Based on previously reported spectroscopic[10-14] and theoretical[15-21] studies, in FOR this is known to directly excite both a member of the 3p Rydberg manifold and a ππ* valence state associated with the C=O group. In DMF and DMA, these absorption bands are red-shifted relative to FOR[12-14] and members of the 3d Rydberg series also become energetically accessible.[20, 22]

II. METHODS

A. EXPERIMENTAL

The experimental setup has been described in detail elsewhere.[23, 24] Pump and probe pulses were derived from the fundamental output of a 1 kHz commercial laser system (Coherent Legend Elite Duo) delivering 35 fs full-width at half-maximum (FWHM) pulses with a central wavelength of 800 nm. A component of this output (0.75 mJ/pulse) was used to generate the probe pulses (267 nm, 2.5 μJ/pulse) by frequency tripling via two consecutive β-barium borate crystals. Pump pulses were generated using a larger fraction of the 800 nm beam (2.75 mJ/pulse), which was further split into two; one part (1.75 mJ/pulse) was frequency tripled to make 267 nm (130 μJ/pulse), while the other part (1 mJ/pulse) was left as the fundamental. These two beams were then focused and overlapped in a shallow non-collinear geometry inside a gas cell containing 40 mbar of Ar, which was slowly replenished by a needle valve-controlled flow. A four-wave mixing scheme, previously demonstrated by Noack and co-workers,[25, 26] produced the fifth harmonic of the fundamental in the VUV region (159.4 nm, estimated at ~0.5 μJ/pulse). This was then separated from the residual 267 nm and 800 nm driving beams using a series of dichroic mirrors with high reflectivity at 160 nm. The VUV

pump and UV probe pulses were focused by separate curved aluminum mirrors before being collinearly overlapped using a final dichroic mirror. As illustrated in detail previously,[23, 24] VUV pump generation and all subsequent beam steering and separation/combination took place inside the gas cell itself, which included a breadboard base for mounting optical components. All opto-mechanical and electrical hardware was selected to be high vacuum compatible to reduce outgassing and hence the presence of hydrocarbon contaminants. The gas cell was coupled directly to the spectrometer via a thin (0.5 mm) CaF2 window, the choice of which resulted in minimal dispersion of the VUV pulse. Temporal delay of the probe relative to the pump (Δt) was controlled by an automated high-precision delay stage placed in the probe beamline.

The velocity-map imaging (VMI) spectrometer utilized for TRPES measurements consisted of differentially pumped molecular beam source and main (interaction) chambers. Seeded gas mixtures were generated by passing 1.3 bars of He carrier gas through a cartridge within a pulsed valve containing small filter paper sections soaked with either FOR, DMF, or DMA (Sigma-Aldrich, >99.5% purity). A molecular beam of the resulting mixture was introduced into the source chamber by a pulsed (1 kHz) Even-Lavie valve (regulated at 60 °C). This was then skimmed (1.0 mm orifice) before entering the interaction region, where multiphoton ionization of the sample by the pump/probe pulses took place between the repeller and extractor lens elements of a VMI electrode assembly. Photoelectrons generated were accelerated along a short flight-tube before impacting upon a 40 mm diameter dual microchannel plate detector backed by a phosphor screen (P47). This was then imaged by a charge-coupled device (CCD) camera via achromatic relay optics. Background subtraction consisted of two corrections: (i) Ionization of residual gas in the main chamber was accounted for by deliberately mistiming the molecular beam and laser pulses at each pump-probe delay and subtracting the resulting signal; (ii) Ionization due to the pump and probe pulses alone was

This manuscript was accepted by J. Chem. Phys. Click here to see the version of record.

removed by subtracting an average of the signals obtained at negative time delays. A fast matrix inversion method was used to process the corrected images,[27] providing data in a form suitable for subsequent angle-, time- and energy-revolved analysis. Representative background subtracted Abel inverted images from pump-probe delays close to $\Delta t = 0$ are presented in Fig. 2. The pump-probe cross-correlation (83-97 fs FWHM) was obtained independently from non-resonant (1+1′) ionization of Xe, and this data was also used for pixel-to-energy calibration. Prior to commencing photoelectron collection, the spectrometer was switched to ion detection mode and the He backing pressure/temperature and timing conditions of the pulsed valve were carefully tuned to ensure no signals from clusters were observed.

Temporal evolution of the angular anisotropy present in the VMI data was analyzed using the appropriate expression for (1 + 1′) ionization with parallel linear polarizations[28-30]

$$I(E,\Delta t,\theta) = \frac{S(E,\Delta t)}{4\pi}[1 + \beta_2(E,\Delta t)P_2(\cos\theta) + \beta_4(E,\Delta t)P_4(\cos\theta)]. \quad (1)$$

Here $P_n(\cos\theta)$ are the n^{th}-order Legendre polynomials, and β_2 and β_4 are the anisotropy parameters describing the shape of the observed photoelectron angular distribution (PAD). The angles $\theta = 0°$ and $180°$ lie along the direction of laser polarization.

A global fitting routine, described previously,[31] was used to model the time-dependent dynamics of the excited molecules. Briefly, angle-integrated photoelectron spectra $S(E, \Delta t)$ are modelled by n exponentially decaying functions $P_i(\Delta t)$ that are convolved with the experimental cross-correlation $g(\Delta t)$

$$S(E,\Delta t) = \sum_{i=1}^{n} A_i(E) \cdot P_i(\Delta t) \otimes g(\Delta t). \quad (2)$$

The global fit returns the $1/e$ decay lifetime τ_i and the energy-dependent amplitudes $A_i(E)$ for each $P_i(\Delta t)$, providing a decay associated spectrum (DAS) attributable to a dynamical process operating on a specific timescale. Since this is a parallel model (i.e. all fit functions originate

This manuscript was accepted by J. Chem. Phys. Click here to see the version of record.

from $\Delta t = 0$), any negative amplitude present in the DAS is indicative of a sequential dynamical process, as detailed elsewhere.[31, 32]

B. COMPUTATIONAL

In support of our experimental work, complementary *ab initio* calculations were implemented using the Gaussian09 package.[33] Ground state geometry evaluations of FOR, DMF and DMA were performed using density functional theory (B3LYP)[34, 35] with an aug-cc-pVTZ basis set. Characterization of these structures as minima was confirmed through analytical Hessian calculations. Vertical singlet excited state energies and (fully relaxed) oscillator strengths were obtained using equation of motion coupled cluster theory including single and double excitations (EOM-CCSD/aug-cc-pVTZ).[36] For comparison, time-dependent density functional theory (TD-DFT) calculations were also undertaken (TD-CAM-B3LYP/aug-cc-pVTZ).[37] Tables I & II summarize the overall results obtained and also include comparisons with various values reported previously in FOR and DMF.

Potential energy cuts along the N-H stretching coordinate of FOR were computed using EOM-CCSD/aug-cc-pVTZ and TD-CAM-B3LYP/aug-cc-pVTZ for the H atom furthest from the amide C=O group. These plots are presented in Fig. 3 (a) and (b), respectively. The qualitative agreement between the two approaches is excellent and, given this outcome, potential cuts along the analogous N-CH_3 coordinate in DMF and the N-CO coordinate in FOR were also then evaluated using the less computationally intensive TD-CAM-B3LYP/aug-cc-pVTZ approach – see Fig. 3 (c) - (d). The rest of the molecular framework was kept rigid throughout bond extension in all cases. Many of the excited states were strongly mixed, making their assignment non-trivial – particularly along the N-CO coordinate. In order to assist with this inherent difficulty, natural transition orbitals (NTOs)[38] were computed at selected critical points along each coordinate (TD-CAM-B3LYP/aug-cc-pVTZ). This enabled dominant excited state orbital contributions to be discerned more definitively. Key observations to

This manuscript was accepted by J. Chem. Phys. Click here to see the version of record.

highlight in Fig. 3 are (i) the dissociative nature of the ππ* state in FOR along the N-CO stretch and (ii) the evolution of σ* valence character in the FOR 3s states at extended N-H distances – something notably absent along the N-CH_3 coordinate of DMF, where instead a member of the 3p Rydberg manifold exhibits this behavior. As highlighted in the Introduction, these differences in Rydberg-to-valence evolution are of considerable interest here. Overall, our calculations suggest that primary and tertiary amides exhibit similar behavior to their aliphatic (rather than aromatic) amine analogues. Given the extensive state mixing, however, such interpretations are challenging – as evident from the differences between our potential cut assignments and those given for DMF by Shastri *et al.* (also using a DFT approach)[22] and Lipciuc *et al*. (using complete active space with second order perturbation theory).[39] Nevertheless, our use of the NTO approach supports the confidence we have in our Rydberg-to-valence analysis over the relatively short-range bond extensions sampled, particularly along the N-H and N-CH_3 bonds.

Experimental photodissociation studies of DMF following 193.3 nm (6.41 eV) excitation have concluded that fragmentation along both the N-CO and N-CH_3 coordinates are energetically open channels.[39-41] This suggests that the absolute energies returned by our present calculations are too high, as the relevant dissociative states are predicted to sit above this point. Where comparisons can be made to experimental values (see Tables I & II), the EOM-CCSD and TD-CAM-B3LYP approaches overestimate the state energies by an average of 0.30 and 0.13 eV, respectively, in FOR and by 0.50 and 0.37 eV in DMF.

III. EXPERIMENTAL RESULTS

A. PHOTOELECTRON SPECTRA

Time-resolved photoelectron spectra are presented in Fig. 4. Given the total available photon energy for (1 + 1′) ionization in our experiment (7.78 eV + 4.65 eV = 12.43 eV), the

expected maximum photoelectron kinetic energy cut-offs for ionization correlating to the cationic ground state in FOR and DMF are 2.21 eV and 3.38 eV, respectively. These values are based on accurately determined adiabatic D_0 ionization potentials (IP) of 10.22 eV and 9.05 eV (see Leach *et al.*[42] and references therein). Small signals extending beyond the predicted cut-offs are due to minor contributions from (1 + 2′) ionization. The adiabatic IP of DMA has not been reported, although the vertical IP (9.09-9.20 eV) is known to be very similar to that of DMF (9.14-9.25 eV).[43-47] This appears to be reflected in the highly comparable DMF and DMA photoelectron spectra. Additionally, we note ionization to the D_1 cation state is also an energetically open channel, as the D_1-D_0 energy separation gap is relatively small (<0.5 eV).[10, 42, 46-48] In FOR, the D_0 and D_1 states are of n^{-1} and π^{-1} character, respectively, whereas this situation is reversed in DMF and DMA.[45-47]

The time-resolved photoelectron spectrum of FOR shows a strong peak centred at 2.1 eV. The narrow width of this feature suggests a significant propensity for $\Delta v = 0$ transitions (where v is a generalized, non-mode-specific vibrational quantum number), indicating this is likely due to Rydberg state ionization.[49] Below 1.8 eV, a broad, mostly unstructured band is prominent, indicative of ionization from a valence state. This broad band is also clearly seen in the time slices presented in the right-hand panels of Fig. 4, but a suggestion of two narrow peaks on top of this broader feature are present at 1.1 eV and 1.4 eV. In contrast, the photoelectron spectrum of DMF shows three distinct narrow bands centered at 2.9 eV, 2.1 eV, and 1.5 eV, with a much less prominent broad band at lower electron kinetic energy. In DMA, two distinct peaks as well as two shoulders, one at high energy and one at low energy, can again be distinguished. The shoulders are situated at 3.3 eV and 1.6 eV, whereas the narrow bands are centered at 2.3 eV and 2.9 eV, respectively. Similar to FOR, the width of the narrow peaks and shoulders suggests ionization from Rydberg states.

In FOR, 159.4 nm (7.78 eV) strongly excites a single member of the 3p Rydberg manifold.[10, 11] Specifically, this is via the n-3p_x transition (see experimental values in Table I) and we assume here this is the only Rydberg transition directly prepared by the pump. This spectral region additionally contains some contributions from $\pi\pi^*$ valence excitation, which gives rise to the broader underlying photoelectron background. The narrow peaks at 1.1 eV and 1.4 eV could suggest lower-lying Rydberg states, based on the aforementioned propensity for $\Delta v = 0$ ionization. Alternatively, they could be due to vibrational structure. As summarized in Table I, the energy gap between the n-3p_x state and the lower-lying n-3s state is ~1 eV, which means that the n-3s state would be expected to exhibit a narrow photoelectron feature at 1.1 eV, exactly matching a peak in the broad lower band of Fig. 4. The lower-lying π-3s state will ionize preferentially to the D_1 cation state, however, as a consequence of Koopmans' correlations[50] and is thus expected at 0.4 eV where no discernible peaks are present. The small peak at 1.4 eV could potentially pertain to the dark π-3p_y state estimated to sit 0.3 eV below the initial excitation by the EOM-CCSD calculations. This would also ionize preferentially to the D_1 cation state, yielding a kinetic energy close to 1.4 eV. There is, however, significant uncertainty associated with the energy of this (dark) state relative to the initially excited state, with different computational methods yielding substantially different relative energies (as indicated in Table I). Any potential internal conversion mechanisms among Rydberg states suggested by the narrow peaks at 1.1 eV and 1.4 eV will be discussed below, following our presentation of a more detailed data analysis.

In the cases of DMF and DMA, definitive assignment of any initially prepared Rydberg states is more challenging than in FOR, although the VUV absorption spectrum of DMF reported by Shastri *et al.* shows that members of the 3d manifold will be predominantly excited.[22] As will be confirmed below by our DAS analysis in Section III. C, 3d excitation would lead directly to the relatively weak ionization feature centred at 2.9 eV, and including

This manuscript was accepted by J. Chem. Phys. Click here to see the version of record.

signal up to the 3.3 eV cut-off (which is associated with vibrationally excited population of this state). The narrow band observed in the temporal slices in Fig. 4 at 1.5 eV in DMF then suggests that internal conversion is to the π-3s Rydberg state, 1.8 eV (3.3 eV – 1.5 eV = 1.8 eV) below the initial excitation (once again assuming a strong $\Delta v = 0$ ionization propensity for Rydberg states). The n-3s Rydberg state is also predicted to give rise to a feature very close this value, at a kinetic energy of 1.4 eV, based on the vertical excitation energy from the absorption spectrum assignment and the propensity for the n-3s state to ionize preferentially to D_1. We note that the high-level EOM-CCSD calculations predict the n-3s state to sit 0.8 eV above the π-3s state, similar to the >0.5 eV gap predicted by the CASPT2 calculations.[39] Assignment of this state based on energetics alone must therefore be taken with considerable caution. The narrow bands at 2.9 eV and 2.1 eV cannot be assigned to specific states, as a congested Rydberg manifold exists below the initial excitation energy. Based on our calculations, the 2.1 eV band most likely corresponds to a 3p state and the 2.9 eV band could be either a 3p or 3d state.

The shoulder at 3.3 eV in DMA corresponds to the initial excitation. Given the similarities between DMA and DMF, this most likely pertains to ionization of a 3d Rydberg state. The lower energy bands at 2.9 eV and 2.3 eV cannot confidently be assigned, but most likely these correspond to ionization from 3p and/or 3d states. The shoulder at 1.6 eV matches the π-3s Rydberg state.

B. PHOTOELECTRON ANGULAR DISTRIBUTIONS (PADs)

The time- and energy-dependence of the β_2 and β_4 parameters obtained from fitting our TRPES data using Eq. 1 are presented in Fig. 5. No clear distinct features are observed in FOR. The diffuse valence band in FOR below 1.8 eV has β_2 and β_4 parameters of 0.6 and 0.0, respectively, consistent with the low anisotropies previously observed for valence states.[5] The β_2 value associated with the sharp Rydberg band in the photoelectron spectrum at 2.1 eV is

This manuscript was accepted by J. Chem. Phys. Click here to see the version of record.

approximately 0.4, with an associated β_4 value close to 0.2. The non-zero β_4 value is consistent with the assignment of ionization from 3p Rydberg state, although the relatively low β_2 anisotropy is somewhat surprising here, considering previous β_2 anisotropies associated with 3p Rydberg state ionization in amines.[5, 6] At a first (i.e., atomic-like) level of approximation, angular momentum conservation ($\Delta l = \pm 1$) means that single-photon ionization of a 3s Rydberg state should only give rise to p photoelectron partial waves and thus a β_4 value of zero.[51] In contrast, however, ionization of atomic-like 3p Rydberg states will give rise to both s and d photoelectron partial waves, with the resulting PAD being dependent on the amplitudes and associated relative phase of these individual contributions. Non-zero β_4 anisotropies are thus consistent with ionization of 3p Rydberg states. The same is true, in principle, for 3d Rydberg states where p and f photoelectron partial waves will be produced. As with p-state ionization, this can clearly yield non-zero β_4 anisotropies, although the significantly larger centrifugal barrier encountered by f partial waves means their overall contribution may be minor relative to the p-wave component, leading to rather small amplitude β_4 contributions close to the ionization threshold.[51] This assertion helps to rationalize why β_4 can be zero in certain cases, although it is important to state this is far from a universal condition (as evidenced, for example, in the Rydberg state ionization of NH_3).[52]

The DMF anisotropy plots show one particularly distinct region of significant photoelectron anisotropy, centered at 2.1 eV and exhibiting β_2 and β_4 values of 0.9 and 0.2, respectively. This is associated with the high intensity 3p/3d Rydberg band also identified in the photoelectron spectrum (see Fig. 4). On either side of the region close to 2.1 eV, the Rydberg state peaks at 2.9 eV (3d) and 1.5 eV (3s) are associated with much lower β_2 values of ~0.5 and β_4 values close to zero. For both the 3s and 3d Rydberg states, this is consistent with the expectations of the simple atomic-like picture of Rydberg state ionization outlined

above. Finally, a similar distinct band, centered at 2.3 eV, is observed in the anisotropy plots for DMA with β_2 and β_4 values up to 1.0 and 0.3, respectively. The band at 2.9 eV and the shoulders at 3.3 eV and 1.6 eV are associated with β_2 values of ~0.5 and β_4 values of 0.0, echoing the observations in DMF that the initially excited 3d Rydberg state and the low-lying 3s Rydberg state are associated with non-zero β_2 values but a β_4 value of zero. In particular, the zero β_4 value of the 3s Rydberg states confirms their assignment and, likewise, the similarities in β_2/β_4 values for the inferred 3d Rydberg states in DMF and DMA strengthen confidence in these assignments.

C. DECAY ASSOCIATED SPECTRA (DAS)

For all molecules considered here, two exponentially decaying functions were required to globally fit the temporal evolution of the observed photoelectron spectra using the procedure described by Eq. 2. The DAS plots obtained are presented in Fig. 6. In order to assess the overall quality of the global fit, the associated residuals (i.e. the fit subtracted from the raw data) are also included. These indicate no serious systematic errors. In all cases, the DAS exhibit extremely fast 10-35 fs (τ_1) and 70-75 fs (τ_2) components. Although these time constants are short relative to the cross-correlations (83-97 fs), these data cannot be described satisfactorily using a simpler, single exponential decay fit (see Fig. 7 for illustrative transient profiles at selected photoelectron kinetic energies). In FOR, both exponential components, in almost equal ratio, appear necessary to describe the evolution of the narrow Rydberg state ionization peak centered at 2.1 eV, whereas the τ_1 = 10 fs component correlates predominantly to decay of photoelectron signals at lower kinetic energy. The τ_1 = 70 fs component has a relatively constant contribution across the band below 1.8 eV. Moreover, the fact that the DAS amplitudes do not display any narrow regions of negative signal indicates no significant internal conversion is occurring between the initially populated n-3p_x state and lower-lying

members of the Rydberg manifold. The likely origin of the narrow peaks observed at 1.1 eV and 1.4 eV are therefore vibrational progressions within the diffuse ππ* valence band.

In contrast to FOR, the overall shapes of the DAS for DMF and DMA exhibit negative amplitudes in the τ_1 component, with narrow, peaked features being clearly visible. This indicates that significant internal conversion processes are occurring within the Rydberg manifolds of DMF and DMA. The timescale associated with this internal conversion are, however, slower (τ_1 = 35 fs for DMF and τ_1 = 30 fs for DMA) than the main decay of the lower-lying lying band in FOR (τ_1 = 10 fs). The decays of the high kinetic energy bands (and thus the initially excited state) are, in all three systems, described by a combination of the two fitted components. This indicates multiple decay pathways out of the initially excited Rydberg state, with neither a purely sequential model nor a purely parallel model fully capturing the dynamics. It appears that only part of the optically prepared population undergoes internal conversion to lower-lying states as described by a sequential model, indicating that an additional deactivation process is operative. The inferred parallel processes are in good agreement with the expectation that the initially excited state has mixed Rydberg-valence character and therefore different dynamical pathways being available for the different excited state characters. These pathways could include partial population transfer to lower-lying Rydberg states, as well as direct dissociation or intramolecular vibrational energy redistribution. Although we note that large amplitude nuclear motion on a single potential energy surface can also induce time-dependent features in photoelectron spectra[53] (which may be misinterpreted within a 2D global fitting model as dynamics evolving across multiple electronic states), we assume this is not a significant factor here. This assertion is based on the narrow spectral features seen in Fig. 4 displaying no energy shift (sweep) towards lower kinetic energy in time, a phenomenon characteristic of large amplitude motion.[53, 54]

This manuscript was accepted by J. Chem. Phys. Click here to see the version of record.

IV. DISCUSION AND CONCLUSION

Following 160 nm excitation, all three amide systems studied exhibit narrow photoelectron peaks which are characteristic of Rydberg state excitation and subsequent ionization. This structure is superimposed on a broader spectral background which we assign to ionization of a ππ* valence state. These observations (Fig. 4) are fully consistent with (i) the previously reported absorption spectra (discussed in the Introduction) and (ii) the theoretical results presented in Tables I and II. The emergent picture is further reinforced by Fig. 5, which reveals that the narrow photoelectron bands in Fig. 4 are associated with narrow regions of high photoelectron anisotropy (consistent with Rydberg state ionization) in DMF and DMA. The orbital character of the various Rydberg states participating in the dynamics cannot be definitively assigned from the PADs, but the energetic regions associated with non-zero β_4 anisotropies are consistent with the position of the assigned 3p Rydberg states. Furthermore, the assignment of narrow photoelectron peaks in DMF and DMA at the expected energies for 3s Rydberg state ionization is corroborated through analysis of the PADs. In particular, the β_4 values of zero at these kinetic energies (see Fig. 5) are in accord with an atomic-like model of photoionization processes. This illustrates the mechanistic value of PADs provided by the highly differential (i.e. energy- and angle-resolved) photoelectron imaging approach.

In DMF and DMA, negative amplitudes observed in the DAS provide clear evidence of sequential dynamics (see τ_1 components in Fig. 6) which we assume are due to ultrafast internal conversion between different excited singlet states (see Fig. 3). The narrow peaks with negative amplitude in Fig. 6 indicate internal conversion within the Rydberg manifold. Additionally, the broad band with negative amplitude superimposed over the narrow peaks in the τ_1 components also indicates internal conversion between the initially excited Rydberg state(s) and states of valence character. Parallel deactivation mechanisms are therefore in operation as the initially excited states are rapidly depopulated. Our calculations suggest one

This manuscript was accepted by J. Chem. Phys. Click here to see the version of record.

parallel pathway leads to extremely rapid fragmentation along either the N-CO or N-CH_3 coordinates in DMF and DMA. Additionally, these calculations indicate that extension along the N-CO coordinate (see panel (c) of Fig. 3) is a critical driver for all possible open dissociation channels, as this motion induces extensive state mixing. Population transfer between members of the 3p/3d Rydberg manifolds and the ππ* valence state are therefore enhanced at relatively short bond extensions (<1.6 Å). The ππ* state also appears to provide a potential route to accessing the lower-lying 3s and nπ* states at more extended N-CO distances. Internal conversion to these states may then potentially compete with direct N-CO bond cleavage, although it appears that, in FOR, dissociation along this coordinate is dominant in that we observed no population of lower-lying Rydberg states. Fig. 6 suggests that internal conversion does not occur to any appreciable extent in FOR, as no negative amplitudes in the DAS were observed. Nevertheless, the initially excited n-$3p_x$ Rydberg state exhibits a fast decay. Since our calculations suggest this state is bound with respect to the two principal dissociation coordinates (Fig. 3), we therefore speculate that internal conversion to either a lower-lying Rydberg state or the ππ* state must still be taking place. This presumably occurs at geometries with extended bond lengths where the probe laser photon energy is no longer sufficient to efficiently ionize the system, and this evolution manifests in an apparent ultrafast decay observed for the n-$3p_x$ state.

For all three systems investigated, we see no evidence of long-lived bound states as Fig. 4 shows no spectral features extending beyond 300 fs. This is perhaps not surprising since rapid, direct dissociation is expected to dominate, given the high photon pump energy (7.78 eV) and the concomitant high levels of vibrational excitation this generates subsequently to internal conversion and/or intramolecular vibrational energy redistribution. This view is further reinforced by the photoelectron spectra in Fig. 4, which clearly display small but non-negligible contributions from (1 + 2′) ionization (which exhibit only rapid (<100fs) dynamics). Higher-

This manuscript was accepted by J. Chem. Phys. Click here to see the version of record.

order photon ionization projects more deeply into the ionization continuum and would be expected to reveal evidence of longer-lived population (if present) in lower-lying states (e.g. triplets and recovery of the S_0 ground state). This is a consequence of Franck-Condon effects being much less restrictive for a (1 + 2′) process than for a (1 + 1′) process. In FOR, the 3s states become dissociative (panels (a) and (b) of Fig. 3) and therefore very short-lived (leading to H atom elimination). We see no direct evidence of this state being populated to any significant extent, however, as no narrow photoelectron peaks observed below 1.8 eV kinetic energy are associated with negative amplitudes in the DAS. As discussed earlier though, we once again stress that this distinct signature may not be visible in our measurements if internal conversion occurs at highly extended bond lengths where valence character dominates and/or the probe photon energy becomes insufficient for ionizing the distorted molecule (as discussed in more detail elsewhere[55]).

For DMF (and, by extension, DMA), our calculations suggest that prompt N-CH_3 dissociation is mediated by σ* valence character developing within the 3p Rydberg manifold. This is in contrast to FOR, where N-H fission occurs via 3s-to-σ* evolution. In both cases, however, some interconversion between different members of the Rydberg manifold is a pre-requisite for dissociation. This is also clearly observed in the TRPES of DMF and DMA. Although extension along the N-CO bond clearly plays a key role in driving the non-adiabatic dynamics here, large amplitude motions of the central carbon atom within the N-C-O plane seems to be less critical, given the very similar dynamical timescales and behavior observed in DMF and DMA (Fig. 6).

In summary, our studies reveal some similarities in the ultrafast relaxation dynamics occurring in FOR, DMF and DMA following 160 nm excitation. Our supporting *ab initio* calculations suggest that all three systems will undergo rapid fragmentation. This is consistent with the very short (<100 fs) excited state lifetimes we observe, although the TRPES

measurement is not able to directly observe the photofragment products. Our calculations also reveal that there are key differences in the mechanisms by which Rydberg-to-valence evolution mediates electronic dynamics in small amide systems upon VUV excitation. In primary amides, 3s Rydberg states appear to play a key role. In contrast, tertiary amides seem to develop dissociative σ* character more readily within the 3p manifold. Although our experiments show clear evidence for internal conversion between multiple Rydberg states in DMF and DMA, the strong preference for ultrafast molecular fragmentation means that we were unable to fully discern subtle differences in their behavior (relative to FOR) at the 160 nm pump wavelength employed. Exciting members of the Rydberg manifold at longer wavelengths (200-170 nm) would likely reveal more about these differences. Although there are presently challenges associated with generating tuneable fs pulses in this spectral region, new source developments in this area will likely overcome this restriction.[56, 57] We conclude that a more complete understanding of the excited state photophysics operating in simple amides must wait for these source developments.

ACKNOWLEDGEMENTS

M.A.B.L. gratefully acknowledges the Oticon Foundation and Knud Højgaards foundation for financial support. M.M.Z. and L.S. acknowledge the support of Heriot-Watt University (HWU) for PhD funding. M.M.Z. also thanks HWU and the University of Ottawa (NSERC) for travel funds. R.F. is grateful to the Engineering and Physical Sciences Research Council (EPSRC) for a research studentship. A.S. thanks the NSERC (Canada) Discovery Grant program for financial support. N.K. was supported on EPSRC Platform Grant EP/P001459/1. We thank Michael S. Schuurman (NRC) for many enlightening discussions on excited state non-adiabatic dynamics.

REFERENCES

1. M. N. R. Ashfold, G. A. King, D. Murdock, M. G. D. Nix, T. A. A. Oliver and A. G. Sage, Phys. Chem. Chem. Phys. **12**, 1218 (2010).
2. G. M. Roberts and V. G. Stavros, Chem. Sci. **5**, 1698 (2014).
3. A. L. Sobolewski, W. Domcke, C. Dedonder-Lardeux and C. Jouvet, Phys. Chem. Chem. Phys. **4**, 1093 (2002).
4. L. B. Klein, T. J. Morsing, R. A. Livingstone, D. Townsend and T. I. Sølling, Phys. Chem. Chem. Phys. **18**, 9715 (2016).
5. L. B. Klein, J. O. F. Thompson, S. W. Crane, L. Saalbach, T. I. Sølling, M. J. Paterson and D. Townsend, Phys. Chem. Chem. Phys. **18**, 25070 (2016).
6. J. O. F. Thompson, L. B. Klein, T. I. Sølling, M. J. Paterson and D. Townsend, Chem. Sci. **7**, 1826 (2016).
7. J. O. F. Thompson, L. Saalbach, S. W. Crane, M. J. Paterson and D. Townsend, J. Chem. Phys. **142**, 114309 (2015).
8. M. M. Zawadzki, M. Candelaresi, L. Saalbach, S. W. Crane, M. J. Paterson and D. Townsend, Faraday Discuss. **194**, 185 (2016).
9. R. J. MacDonell, O. Schalk, T. Geng, R. D. Thomas, R. Feifel, T. Hansson and M. S. Schuurman, J. Chem. Phys. **145**, 114306 (2016).
10. D. H. A. ter Steege, C. Lagrost, W. J. Buma, D. A. Leigh and F. Zerbetto, J. Chem. Phys. **117**, 8270 (2002).
11. J. M. Gingell, N. J. Mason, H. Zhao, I. C. Walker and M. R. F. Siggel, Chem. Phys. **220**, 191 (1997).
12. H. Basch, M. B. Robin and N. A. Kuebler, J. Chem. Phys. **49**, 5007 (1968).
13. K. Kaya and S. Nagakura, Theor. Chim. Acta **7**, 117 (1967).
14. H. D. Hunt and W. T. Simpson, J. Am. Chem. Soc. **75**, 4540 (1953).
15. D. P. Chong, J. Electron. Spectrosc. Relat. Phenom. **184**, 164 (2011).
16. I. Antol, M. Barbatti, M. Eckert-Maksić and H. Lischka, Monatsh. Chem. **139**, 319 (2008).
17. I. Antol, M. Barbatti, M. Eckert-Maksić and H. Lischka, J. Chem. Phys. **127**, 234303 (2007).
18. I. Antol, M. Eckert-Maksić and H. Lischka, J. Phys. Chem. A **108**, 10317 (2004).
19. P. G. Szalay and G. Fogarasi, Chem. Phys. Lett. **270**, 406 (1997).
20. L. Serrano-Andrés and M. P. Fülscher, J. Am. Chem. Soc. **118**, 12190 (1996).
21. J. D. Hirst, D. M. Hirst and C. L. Brooks, J. Phys. Chem. **100**, 13487 (1996).
22. A. Shastri, A. K. Das, S. Krishnakumar, P. J. Singh and B. N. R. Sekhar, J. Chem. Phys. **147**, 224305 (2017).
23. M. R. Coates, M. A. B. Larsen, R. Forbes, S. P. Neville, A. E. Boguslavskiy, I. Wilkinson, T. I. Sølling, R. Lausten, A. Stolow and M. S. Schuurman, J. Chem. Phys. **149**, 144311 (2018).
24. R. Forbes, V. Makhija, K. Veyrinas, A. Stolow, J. W. L. Lee, M. Burt, M. Brouard, C. Vallance, I. Wilkinson, R. Lausten and P. Hockett, J. Chem. Phys. **147**, 013911 (2017).
25. M. Beutler, M. Ghotbi, F. Noack and I. V. Hertel, Opt. Lett. **35**, 1491 (2010).
26. M. Ghotbi, M. Beutler and F. Noack, Opt. Lett. **35**, 3492 (2010).

27. R. Livingstone, A., J. O. F. Thompson, M. Iljina, R. J. Donaldson, B. J. Sussman, M. J. Paterson and D. Townsend, J. Chem. Phys. **137**, 184304 (2012).

28. K. L. Reid, Annu. Rev. Phys. Chem. **54**, 397 (2003).

29. T. Suzuki, Annu. Rev. Phys. Chem. **57**, 555 (2006).

30. A. Stolow and J. G. Underwood, Adv. Chem. Phys. **139**, 497 (2008).

31. O. Schalk, A. E. Boguslavskiy and A. Stolow, J. Phys. Chem. A **114**, 4058 (2010).

32. G. Wu, A. E. Boguslavskiy, O. Schalk, M. S. Schuurman and A. Stolow, J. Chem. Phys. **135**, 164309 (2011).

33. M. J. Frisch, G. W. Trucks, H. B. Schlegel, G. E. Scuseria, M. A. Robb, J. R. Cheeseman, G. Scalmani, V. Barone, B. Mennucci, G. A. Petersson, H. Nakatsuji, M. Caricato, X. Li, H. P. Hratchian, A. F. Izmaylov, J. Bloino, G. Zheng, J. L. Sonnenberg, M. Hada, M. Ehara, K. Toyota, R. Fukuda, J. Hasegawa, M. Ishida, T. Nakajima, Y. Honda, O. Kitao, H. Nakai, T. Vreven, J. J. A. Montgomery, J. E. Peralta, F. Ogliaro, M. Bearpark, J. J. Heyd, E. Brothers, K. N. Kudin, V. N. Staroverov, R. Kobayashi, J. Normand, K. Raghavachari, A. Rendell, J. C. Burant, S. S. Iyengar, J. Tomasi, M. Cossi, N. Rega, J. M. Millam, M. Klene, J. E. Knox, J. B. Cross, V. Bakken, C. Adamo, J. Jaramillo, R. Gomperts, R. E. Stratmann, O. Yazyev, A. J. Austin, R. Cammi, C. Pomelli, J. W. Ochterski, R. L. Martin, K. Morokuma, V. G. Zakrzewski, G. A. Voth, P. Salvador, J. J. Dannenberg, S. Dapprich, A. D. Daniels, O. Farkas, J. B. Foresman, J. V. Ortiz, J. Cioslowski and D. J. Fox, Gaussian09 Revision D.01. Gaussian Inc. Wallingford CT (2013).

34. A. D. Becke, J. Chem. Phys. **98**, 5648 (1993).

35. P. J. Stephens, F. J. Devlin, C. F. Chabalowski and M. J. Frisch, J. Phys. Chem. **98**, 11623 (1994).

36. H. Koch and P. Jørgensen, J. Chem. Phys. **93**, 3333 (1990).

37. T. Yanai, D. P. Tew and N. C. Handy, Chem. Phys. Lett. **393**, 51 (2004).

38. R. L. Martin, J. Chem. Phys. **118**, 4775 (2003).

39. M. L. Lipciuc, S. H. Gardiner, T. N. V. Karsili, J. W. L. Lee, D. Heathcote, M. N. R. Ashfold and C. Vallance, J. Chem. Phys. **147**, 013941 (2017).

40. N. R. Forde, L. J. Butler and S. A. Abrash, J. Chem. Phys. **110**, 8954 (1999).

41. N. R. Forde, T. L. Myers and L. J. Butler, Faraday Discuss. **108**, 221 (1997).

42. S. Leach, N. Champion, H.-W. Jochims and H. Baumgärtel, Chem. Phys. **376**, 10 (2010).

43. M. A. Baldwin, A. G. Loudon, K. S. Webb and P. C. Cardnell, Org. Mass Spectrom. **12**, 279 (1977).

44. G. Bieri, L. Åsbrink and W. von Niessen, J. Electron Spectros. Relat. Phenom. **27**, 129 (1982).

45. C. R. Brundle, D. W. Turner, M. B. Robin and H. Basch, Chem. Phys. Lett. **3**, 292 (1969).

46. L. Henriksen, R. Isaksson, T. Liljefors and J. Sandström, Acta Chem. Scand. **B35**, 489 (1981).

47. D. A. Sweigart and D. W. Turner, J. Am. Chem. Soc. **94**, 5592 (1972).

48. H. Siegbahn, L. Asplund, P. Kelfve, K. Hamrin, L. Karlsson and K. Siegbahn, J. Electron. Spectrosc. Relat. Phenom. **5**, 1059 (1974).

49. S. T. Pratt, Rep. Prog. Phys. **58**, 821 (1995).

50. V. Blanchet, M. Z. Zgierski and A. Stolow, J. Chem. Phys. **114**, 1194 (2001).

51. G. Wu, P. Hockett and A. Stolow, Phys. Chem. Chem. Phys. **13**, 18447 (2011).

52. P. Hockett, M. Staniforth, K. L. Reid and D. Townsend, Phys. Rev. Lett. **102**, 253002 (2009).

53. A. E. Boguslavskiy, O. Schalk, N. Gador, W. J. Glover, T. Mori, T. Schultz, M. S. Schuurman, T. J. Martínez and A. Stolow, J. Chem. Phys. **148**, 164302 (2018).

54. S. P. Neville, Y. Wang, A. E. Boguslavskiy, A. Stolow and M. S. Schuurman, J. Chem. Phys. **144**, 014305 (2016).

55. M. M. Zawadzki, J. O. F. Thompson, E. A. Burgess, M. J. Paterson and D. Townsend, Phys. Chem. Chem. Phys. **17**, 26659 (2015).

56. P. S. J. Russell, P. Hölzer, W. Chang, A. Abdolvand and J. C. Travers, Nat. Photonics **8**, 278 (2014).

57. M. Ghotbi, P. Trabs, M. Beutler and F. Noack, Opt. Lett. **38**, 486 (2013).

58. G. Fogarasi, J. Mol. Struct. **978**, 257 (2010).

TABLE CAPTIONS

Table I: Calculated vertical excitation energies in eV (with associated oscillator strengths in parentheses). For comparison, theory data from several sources (employing a range of different computational strategies) is also included, along with known experimental values. States are heavily mixed, but at the equilibrium geometry considered here the largest individual orbital contribution is typically >50%. The *x*, *y* and *z* labels for p Rydberg states follow standard Gaussian09 molecular orientation conventions, although orbitals are not directed fully along these axes and assignments are for approximate guidance only.

Table II: Calculated vertical excitation energies in eV (with associated oscillator strengths in parentheses). States are heavily mixed, but at the equilibrium geometry considered here the largest individual orbital contribution is typically >50%. The *x*, *y* and *z* labels for p Rydberg states follow standard Gaussian09 molecular orientation conventions, although orbitals are not directed fully along these axes and assignments are for approximate guidance only.

Table I

FOR	Present Work		Previous Work					
	1	2	A	B	C	D	E	F (Expt.)
$n\rightarrow\pi^*$	5.72 (0.001)	5.62 (0.001)	5.71 (0.001)	5.78 (0.001)	5.71 (0.000)	5.86 (0.000)	5.61 (0.001)	5.82
$\pi\rightarrow 3s$	6.91 (0.021)	6.72 (0.017)	7.32 (0.021)	6.77 (0.021)	6.73 (0.021)	6.14 (0.022)	6.52 (0.024)	6.35
$n\rightarrow 3s$	7.00 (0.001)	6.75 (0.004)	6.64 (0.009)	6.78 (0.006)	6.81 (0.002)	6.49 (0.000)	6.59 (0.003)	-
$n\rightarrow 3p_y$	7.56 (0.136)	7.28 (0.066)	7.42 (0.085)	7.47 (0.058)	7.38 (0.072)	7.16 (0.060	7.31 (0.065)	7.40
$\pi\rightarrow 3p_y$	7.76 (0.001)	7.49 (0.001)	8.07 (0.016)	7.62 (0.000)	7.59 (0.001)	7.01 (0.001)	7.04 (0.000)	-
$\pi\rightarrow\pi^*$	7.79 (0.232)	7.81 (0.211)	7.77 (0.282)	7.71 (0.338)	7.66 (0.211)	7.94 (0.149)	7.41 (0.371)	7.36
$n\rightarrow 3p_x$	8.06 (0.060)	7.64 (0.093)	8.25 (0.008)	7.84 (0.017)	7.88 (0.064)	7.50 (0.041)	7.73 (0.022)	7.72
$\pi\rightarrow 3p_x$	8.34 (0.006)	8.09 (0.008)	8.95 (0.005)	8.03 (0.001)	8.17 (0.008)	7.57 (0.005)	7.97 (0.007)	8.02
$n\rightarrow 3p_z$	8.39 (0.006)	8.11 (0.004)	9.01 (0.026)	8.08 (0.013)	8.20 (0.006)	7.47 (0.005)	7.81 (0.005)	7.83
$\pi\rightarrow 3p_z$	8.68 (0.007)	8.51 (0.009)	9.60 (0.009)	8.28 (0.033)	8.52 (0.006)	7.40 (0.136)	7.72 (0.101)	8.22

1: EOM-CCSD/aug-cc-pVTZ
2: TD-CAM-B3LYP/aug-cc-pVTZ

A: TD-SAOP/CCSD(T)[15]
B: MR-CISD+Q/d′-aug-cc-pVDZ[18]
C: EOM-CCSD/PBS[19]
D: CASSCF/MR-CI/6-31+G**[21]
E: CASSCF/CASPT2/ANO-2[4s3p1d/2s][20]
F: VUV absorption data[11]

Table II

DMF	Present Work		Previous Work			DMA	Present Work	
	1	2	A	B	C (Expt.)		1	2
$n\rightarrow\pi^*$	5.81 (0.001)	5.69 (0.001)	5.59 (0.000)	5.64 (0.001)	5.57	$n\rightarrow\pi^*$	5.85 (0.001)	5.74 (0.001)
$\pi\rightarrow 3s$	6.21 (0.016)	6.13 (0.022)	5.62 (0.021)	5.92 (0.005)	5.96	$\pi\rightarrow 3s$	5.99 (0.017)	5.96 (0.023)
$\pi\rightarrow\pi^*$	6.69 (0.184)	6.64 (0.127)	6.32 (0.108)	6.50 (0.365)	6.24	$n\rightarrow 3s$	6.69 (0.022)	6.51 (0.018)
$\pi\rightarrow 3p_y$	6.99 (0.005)	6.89 (0.005)	6.28 (0.004)	6.77 (0.001)	6.54	$\pi\rightarrow 3p_x$	6.81 (0.005)	6.72 (0.005)
$n\rightarrow 3s$	7.05 (0.021)	6.83 (0.051)	5.99 (0.009)	6.48 (0.002)	6.12	$\pi\rightarrow 3p_z$	6.81 (0.085)	6.78 (0.127)
$\pi\rightarrow 3p_x$	7.14 (0.001)	7.06 (0.001)	6.49 (0.000)	6.63 (0.002)	6.74	$\pi\rightarrow 3p_y$	6.88 (0.001)	6.85 (0.002)
$\pi\rightarrow 3p_z$	7.40 (0.078)	7.38 (0.054)	7.00 (0.068)	6.55 (0.004)	6.90	$\pi\rightarrow\pi^*$	6.92 (0.204)	6.92 (0.115)
$\pi\rightarrow 3d_z^2$	7.51 (0.001)	7.42 (0.001)	6.91 (0.000)	7.24 (0.000)	-	$\pi\rightarrow 3d_{xy}$	7.31 (0.001)	7.25 (0.000)
$n\rightarrow 3p_y$	7.71 (0.028)	7.41 (0.026)	6.59 (0.017)	7.09 (0.010)	6.97	$n\rightarrow 3p_x$	7.47 (0.006)	7.22 (0.005)

1: EOM-CCSD/aug-cc-pVTZ
2: TD-CAM-B3LYP/aug-cc-pVTZ

A: TD-B3LYP/aug-cc-pVTZ[22]
B: CASSCF/CASPT2/ANO-2[4s3p1d/2s][20]
C: VUV absorption data[22]

FIGURE CAPTIONS

Figure 1: Schematic structures of all three amide species studied. On the basis of previously reported *ab initio* calculations (see[58] and references therein), we may assume no tautomers other than the keto forms depicted here will be present under our experimental conditions.

Figure 2: (1 + 1′) photoelectron images obtained for all three amide systems at pump–probe delay times close to $\Delta t = 0$. Unwanted background signals have been subtracted (see main text for more details) and the images are 4-fold symmetrized. The images have also been subjected to a matrix inversion procedure, described in Ref.[27]. The (linear) polarization direction of the 160 nm pump and 267 nm probe beams is vertical with respect to the figure.

Figure 3: Diabatic potential energy cuts along selected N-X bonds in FOR (a) – (c) and DMF (d). State assignments in the inset panel of (a) also apply to (b) and (c). Assignments are based on the largest individual orbital character in the vertical Franck-Condon region. For additional details, see the main text.

Figure 4: (Left) 2D time-dependent photoelectron spectra of FOR, DMF and DMA obtained using a 160/267 nm pump/probe. White vertical dashed lines (FOR and DMF only) denote predicted (1+1′) energy cut-offs, as discussed in the main text. (Right) energy slices though the 2D data at selected pump-probe delay times. Multiple narrow peaks superimposed on a broader background are clearly visible in DMF and DMA.

Figure 5: 2D photoelectron anisotropy parameter plots obtained for FOR, DMF and DMA using a 160 nm pump and 267 nm probe. Plots are limited to regions of the TRPES data with

>5 % of the maximum recorded signal. The energy-resolved photoelectron spectrum at close to zero pump-probe delay is also overlaid in each case.

Figure 6: Left hand panels show decay associated spectra (DAS) obtained from 2D global multi-exponential fits to the data presented in Fig. 4. For additional details, see main text. Quoted decay lifetimes in τ_1 and τ_2 have 1σ uncertainties of ± 15%. Right hand panels show 2D plots of the fit residuals (i.e. the global fit subtracted from the raw data).

Figure 7: Transient profile data for FOR (left) and DMF (right), each at two different photoelectron kinetic energies. Also included are overlays illustrating Gaussian cross-correlation functions $g(\Delta t)$. These are 85 fs and 90 fs FWHM for FOR and DMF, respectively (as used in our global fitting analysis). For comparative purposes, data have been intensity normalized. The transients for DMA are very similar to those for DMF (at the same kinetic energy) and so are not shown.

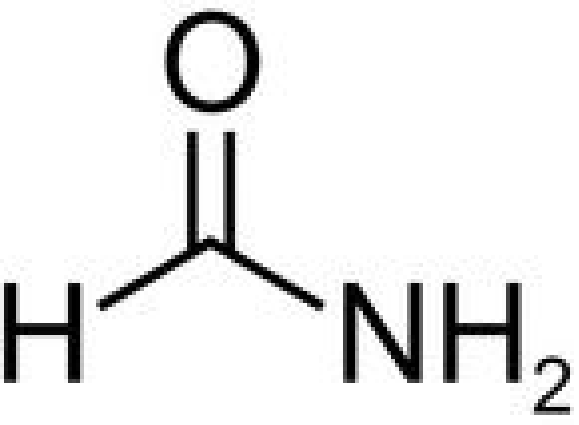

Formamide
(FOR)

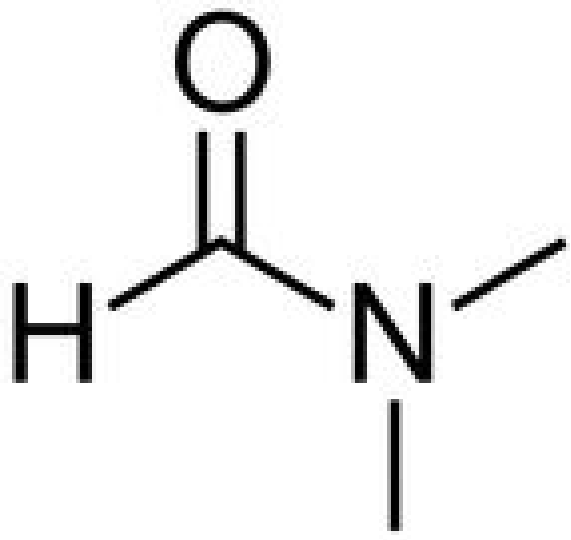

N,*N*-dimethylformamide
(DMF)

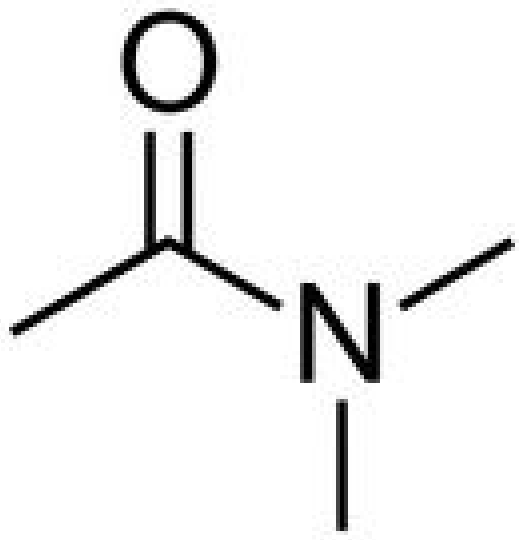

N,*N*-dimethylacetamide
(DMA)

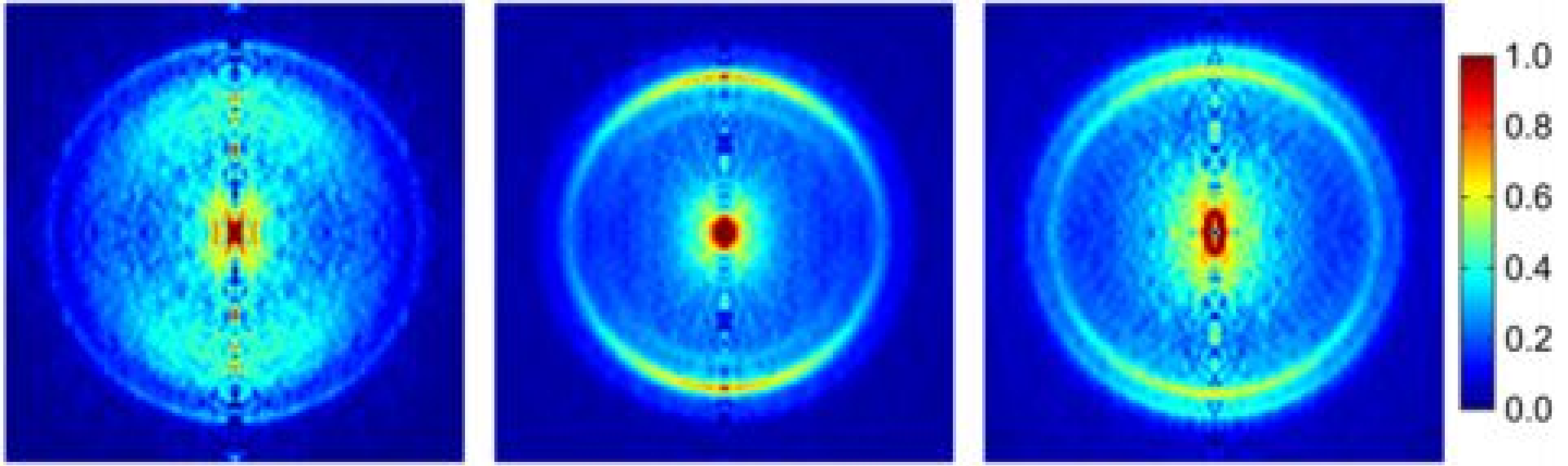

FOR DMF DMA

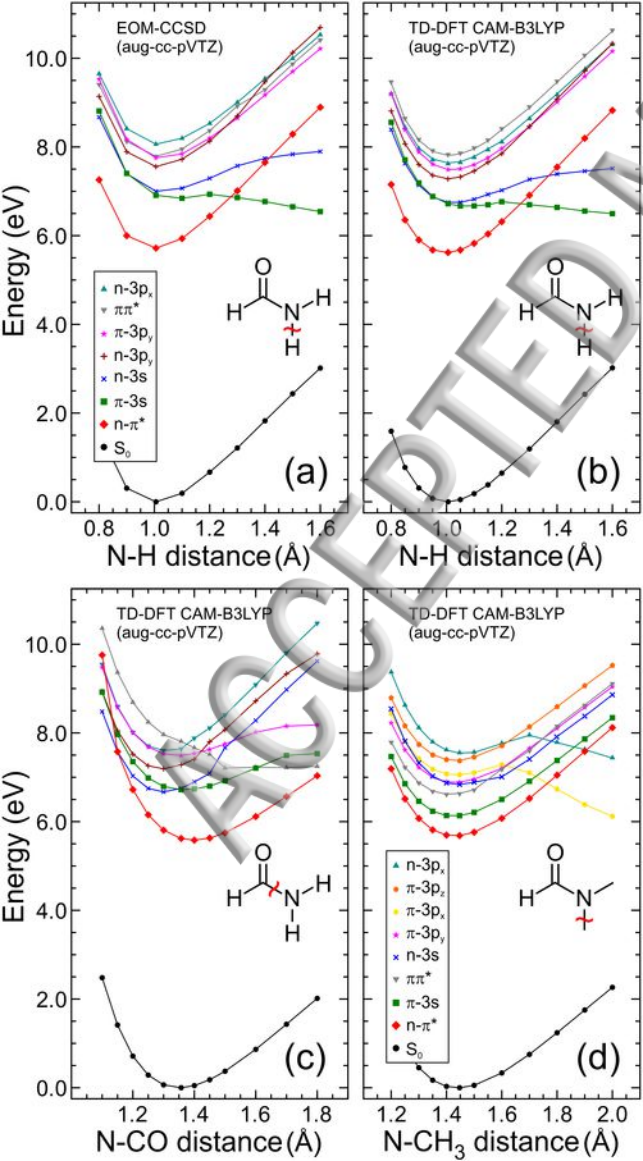
EOM-CCSD
(aug-cc-pVTZ)
TD-DFT CAM-B3LYP
(aug-cc-pVTZ)
TD-DFT CAM-B3LYP
(aug-cc-pVTZ)
TD-DFT CAM-B3LYP
(aug-cc-pVTZ)
Energy (eV)
N-H distance (Å)
N-H distance (Å)
N-CO distance (Å)
N-CH3 distance (Å)
n-3px
ππ*
π-3py
π-3pz
n-3s
π-3s
n-π*
S0
(a)
(b)
(c)
(d)

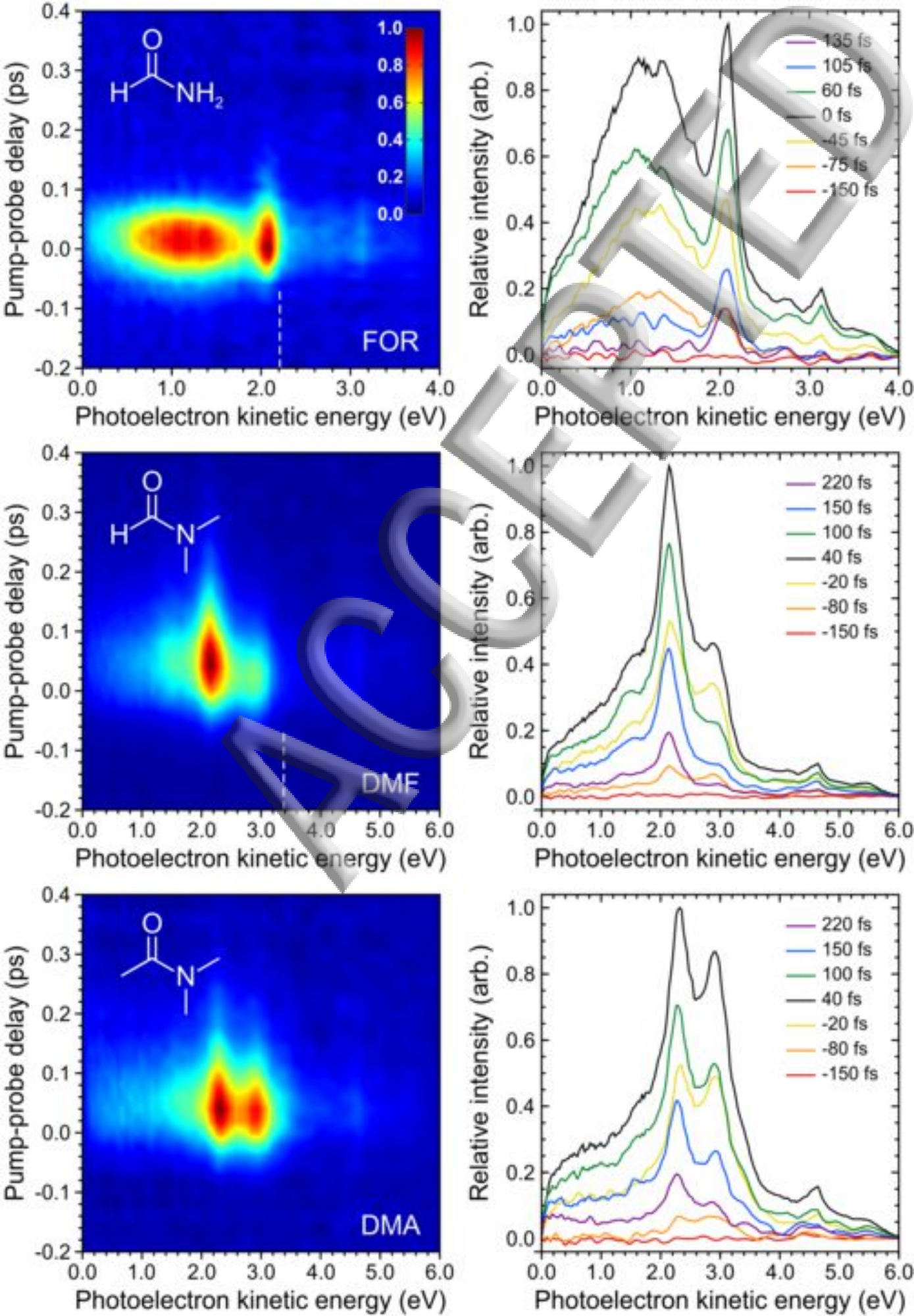
Pump-probe delay (ps)
Photoelectron kinetic energy (eV)
Relative intensity (arb.)
FOR
DMF
DMA
135 fs
105 fs
60 fs
0 fs
-45 fs
-75 fs
-150 fs
220 fs
150 fs
100 fs
40 fs
-20 fs
-80 fs
-150 fs

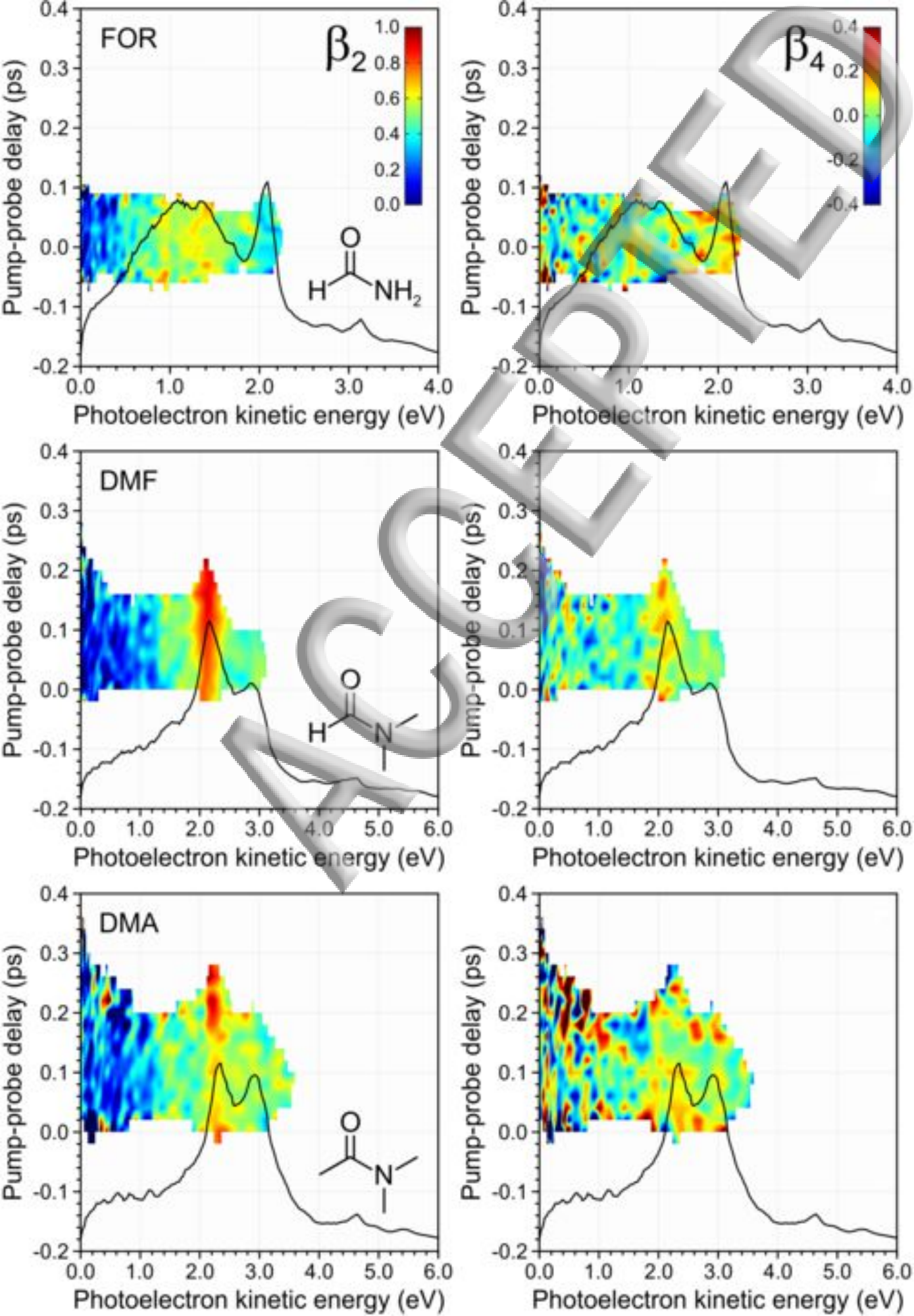
FOR
β_2
β_4
DMF
DMA
Pump-probe delay (ps)
Photoelectron kinetic energy (eV)
H
O
NH2
N

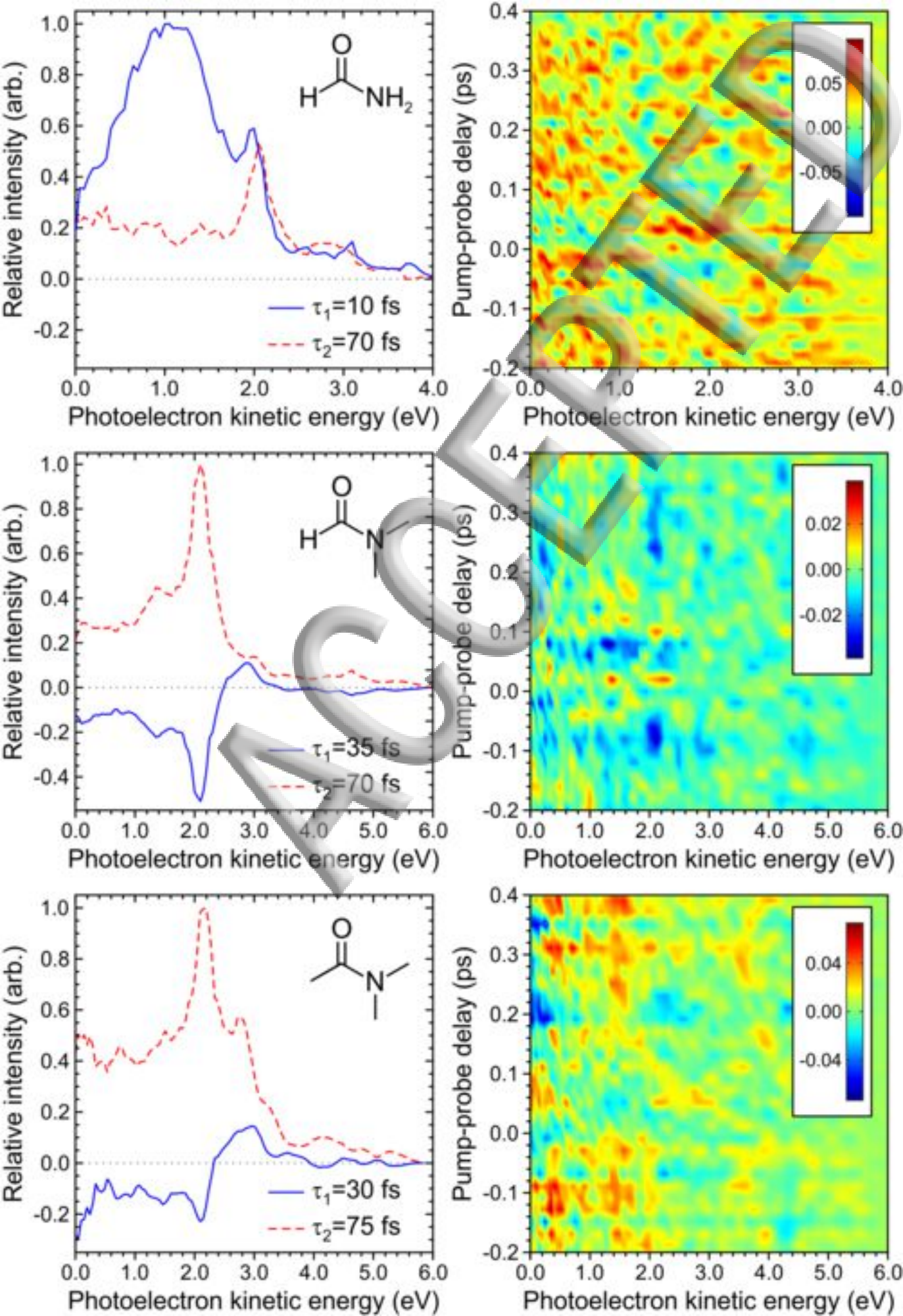
Relative intensity (arb.)
Photoelectron kinetic energy (eV)
Pump-probe delay (ps)
τ1=10 fs
τ2=70 fs
τ1=35 fs
τ2=70 fs
τ1=30 fs
τ2=75 fs
O
H
NH2
N
0.05
0.00
-0.05
0.02
0.00
-0.02
0.04
0.00
-0.04

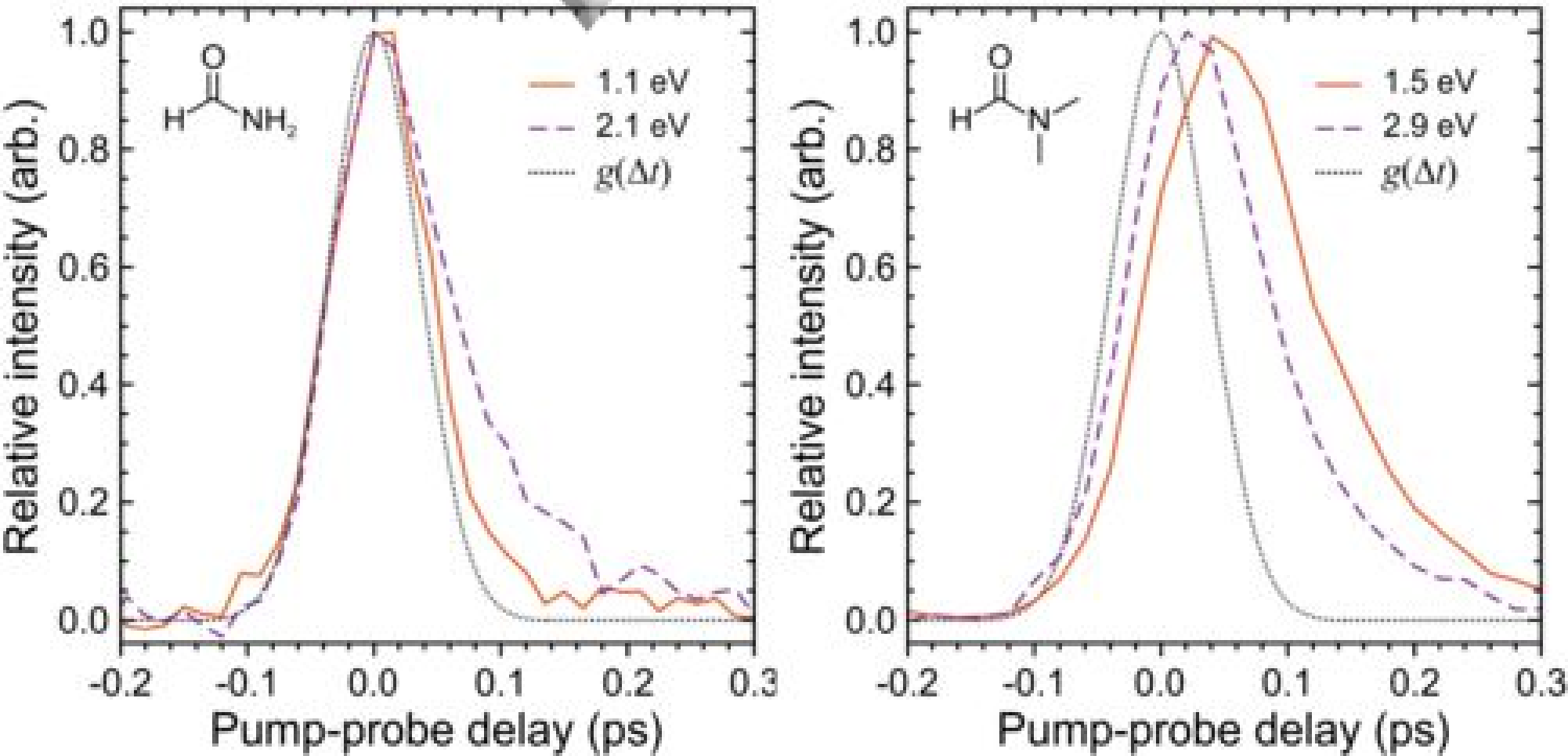
1.0
0.8
0.6
0.4
0.2
0.0
Relative intensity (arb.)
-0.2
-0.1
0.0
0.1
0.2
0.3
Pump-probe delay (ps)
O
H
NH2
1.1 eV
2.1 eV
g(Δt)
1.5 eV
2.9 eV
N